



HAL
open science

Bichromatic melt pool thermal measurement based on a Red, Green, and Blue camera: Application to additive manufacturing processes

Loïc Jegou, Joel Lachambre, Nicolas Tardif, Mady Guillemot, Anthony Dellarre, Abderrahime Zaoui, Thomas Elguedj, Valérie Kaftandjian, Nicolas Béraud

► To cite this version:

Loïc Jegou, Joel Lachambre, Nicolas Tardif, Mady Guillemot, Anthony Dellarre, et al.. Bichromatic melt pool thermal measurement based on a Red, Green, and Blue camera: Application to additive manufacturing processes. *Optics and Laser Technology*, 2023, 167, pp.109799. 10.1016/j.optlastec.2023.109799 . hal-04209790

HAL Id: hal-04209790

<https://hal.science/hal-04209790v1>

Submitted on 23 Dec 2024

HAL is a multi-disciplinary open access archive for the deposit and dissemination of scientific research documents, whether they are published or not. The documents may come from teaching and research institutions in France or abroad, or from public or private research centers.

L'archive ouverte pluridisciplinaire **HAL**, est destinée au dépôt et à la diffusion de documents scientifiques de niveau recherche, publiés ou non, émanant des établissements d'enseignement et de recherche français ou étrangers, des laboratoires publics ou privés.



Distributed under a Creative Commons Attribution 4.0 International License

Highlighted review - Bichromatic melt pool thermal measurement based on a Red, Green, and Blue camera: application to additive manufacturing processes

Loïc Jegou^{a,b,*}, Joel Lachambre^a, Nicolas Tardif^a, Mady Guillemot^a, Anthony Dellarre^c, Abderrahime Zaoui^a, Thomas Elguedj^a, Valerie Kaftandjian^b and Nicolas Beraud^c

^aUniv. Lyon, INSA Lyon, CNRS, Lamcos, UMR5259, 69100, Villeurbanne, France

^bUniv. Lyon, INSA Lyon, LVA, 69100, Villeurbanne, France

^cUniv. Grenoble Alpes, CNRS, Grenoble INP, G-SCOP, 38000, Grenoble, France

ARTICLE INFO

Keywords:

Bichromatic thermometer
Direct energy deposition
Laser metal deposition with powder
Wire arc additive manufacturing
Thermal imaging
Melt pool identification

ABSTRACT


The measure of temperature fields during additive manufacturing processes usually requires bulky expansive equipment such as infrared cameras. The full field sensor introduced in this paper is very compact and made with a single red, green and blue camera. Based on a dual-wavelength radiometric model, it is designed to measure temperatures ranging from 1000 to 2500 K. With its dynamic exposure time feature, it rearranges multiple pictures in a median one to observe phenomena with high thermal gradients. The precision of the measures is ensured by calibration on a black body and a tungsten ribbon lamp. The method is applied to wire arc additive manufacturing and laser metal deposition with powder, and accurate measurement of the thermal gradients in the melt pool and the surrounding solid phase is achieved. The good resolution of the camera gives an accurate insight of the melt pool shape and size.

1. Introduction

Additive Manufacturing (AM) processes for metal parts are a technology that has been growing constantly for the past 10 years and was regarded as the new industrial revolution (Berman [1]). It consists in creating an object by continuously depositing new material, layer by layer. An exhaustive review of the different types of AM processes and their challenges has been written by Frazier [2]. This paper primarily focuses on two processes of the Direct Energy Deposition (DED) branch, Laser Metal Deposition with Powder (LMD-p) and Wire Arc Additive Manufacturing (WAAM). The first one consists of melting a small section of a substrate with a highly focused energy source, and continuously delivering feedstock material in this melt pool in the form of powder or wire, layer by layer. Svetlizky et al. [3] gives an exhaustive review of LMD-p and LMD-wire processes. The second one is more widespread and fitted to produce large parts (>10 kg) with a greater variety of metals (Williams et al. [4]). It is based on gas metal arc welding processes and consists of melting a metal wire onto the substrate with an electric arc as the heat source (Wu et al. [5]). These processes have a lot of input parameters that impact the mechanical properties of the printed object (Lewandowski and Seifi [6]). An exhaustive list of the anomalies and their causes that can occur during DED processes was detailed by Liu et al. [7]. A lot of these irregularities are due to the

process parameters (*e.g.* the powder flowrate, the scanning speed of the robot, its trajectory...) and the fast-growing of machine learning helped to better choose optimal parameters to reduce defects (Wang et al. [8] and Johnson et al. [9]).

Although these techniques provide a convenient environment to work in, they can not guarantee a part without defects due to the complexity of the underlying physics in the liquid zone, called the melt pool. It critically impacts the final quality of the manufactured part and is a very reliable indicator of defect formation (Scime and Beuth [10]). Yuan et al. [11] identified 4 states of the melt pool which lead to potential defects: over melting, normal melting, incomplete melting, and discontinuity melting. If it is too wide and deep (*i.e.* the energy source is too high or its velocity too slow) it can result in keyhole porosity while a shallow melt pool will lead to a lack of fusion and also porosity or bulking. Thus it is interesting to keep track of the melt pool during the production of a part. There are different ways to observe this area: punctual or wide field of view with a coarse or fine resolution, in the visible or infrared waveband... For instance, Jeon et al. [12] used an infrared camera coupled with an artificial neural network to estimate the depth of the melt pool during the fabrication. Porosity prediction during AM processes has also been investigated by Khanzadeh et al. [13] based on thermal imaging of the melt pool, but also with ultrasonic approaches by Eren et al. [14]. In WAAM, which is a faster process, heat accumulation is a recurring problem that leads to wider depositions for the top layers (Wu et al. [15]). Finally, although most DED methods require a shielding gas to prevent oxidation around the melt pool, it is an additional source of anomalies since oxides remelt to enter the melt pool and act as impurities

 loic.jegou@insa-lyon.fr (L. Jegou); joel.lachambre@insa-lyon.fr (J. Lachambre); nicolas.tardif@insa-lyon.fr (N. Tardif); mady.guillemot@insa-lyon.fr (M. Guillemot); anthony.dellarre@grenoble-inp.fr (A. Dellarre); abderrahime.zaoui@insa-lyon.fr (A. Zaoui); thomas.elguedj@insa-lyon.fr (T. Elguedj); valerie.kaftandjian@insa-lyon.fr (V. Kaftandjian); nicolas.beraud@grenoble-inp.fr (N. Beraud)

(Hauser et al. [16]). Thus there is a great interest in analyzing and observing the melt pool during the fabrication of a part. Modelisation of the melt pool at different scales (Cook and Murphy [17]) with mathematical models (Fathi et al. [18]), coupled analytical and numerical models (Peyre et al. [19]), finite element methods (Michaleris [20], Baykasoglu et al. [21], Stender et al. [22], Heigel et al. [23]) or data-driven models (Akbari et al. [24]) also provides lines of research to reduce defects formations. However the simulated phenomena are highly complex, and direct observation is a more reliable way of monitoring the melt pool.

Unlike contact measurements, that by their intrusive nature often induce a significant error (Jailin et al. [25]), non-intrusive methods have been widely used in the AM industry.

For instance, radioscopy is a powerful non-intrusive method using x-rays to observe the inside of an object: Wolff and Gould [26] and Boley et al. [27] coupled it with optical imaging to get the melt pool geometry inside the part being produced. However, these are very expensive and bulky installations.

It is possible to resort only to optical imaging of the surface of the melt pool to monitor its shape (Sun et al. [28], Gibson et al. [29], Ding et al. [30], Smurov et al. [31] in DED with powder and Zhao et al. [32], Xiong et al. [33] in WAAM).

Identifying the shape of the melt pool can be challenging on red, green and blue (RGB) or gray-level pictures since there are no obvious boundaries. That's why optical imaging is often coupled to thermal imaging in the AM domain. The transition temperature of a material between its solid and liquid phases is known, and thermal cartography of the melt pool provides a simple solution to draw its contour.

The most common answer to thermal observations is infrared cameras. Although Everton et al. [34] wrote that these solutions are often limited by their field of view or resolution, these limits are challenged by high-quality components. For instance in LMD-p, Liu et al. [35] used one to record the thermal behavior of the melt pool and get an accurate 3D temperature profile. And during gas tungsten arc and gas metal arc welding (that are close to WAAM in terms of temperature), Yamazaki et al. [36] obtained the complete thermal cartography of the melt pool with temperatures ranging from 1900 K near the edges of the liquid zone to 2900 K at the center in gas tungsten arc.

However, infrared cameras are usually bulky (*i.e.* not easily adaptable to any experiment), and expensive compared to Complementary Metal Oxide Semiconductor (CMOS) or Charge-Coupled Device (CCD) cameras with the same resolution.

Thermal imaging is also feasible in the near-infrared as it has been done in other domains by Rotrou et al. [37] to measure temperatures ranging from 600 K to 1000 K and even above 1300 K (Jailin et al. [38]). It is also achievable in the visible waveband since the principle is the same. All these methods resort to either pyrometry or spectroscopy. Schöpp et al. [39] wrote a review on

methods based on either one or the other, and highlighted that the emissivity of the observed surface is a key factor in the temperature estimation. In DED processes, Kozakov et al. [40] reported that it varies near the melt pool and decreases when the temperature increases. They used optical emission spectroscopy to punctually measure the emissivity and the temperature, and then find a linear relationship between these values. This relation is then used with a high-speed camera to reconstruct the thermal cartography of the melt pool. These studies rely on modeling the emissivity, which has to be done for each orientation of the surface (respectively to the camera), each material, and each specific process: tungsten inert gas and cold metal transfer welding. Besides, the uncertainties induced by slag formation and the state of the material (liquid, solid, or in the transition zone) have not been investigated and might distort the computed temperature. A way to overcome the emissivity issue is to use two colors spectroscopy (or pyrometry). It consists in measuring the ratio of two radiances at two different wavelengths and assuming that the emissivity is constant over a certain wavelength range (which means that the emissivity ratio is equal to 1).

Khan et al. [41] introduced the basics of two, three, and four colors pyrometry. It is shown that there is no advantage in using more than two colors and most studies nowadays resort to bi-color pyrometry. Besides, Duvaut [42] showed that multi-wavelength pyrometry is more powerful in the visible range than in the infrared.

Monier et al. [43] set up a two-color pyrometer to study the temperature of liquid metals. It is made of two CCD cameras mounted on an optical device with a divergence mirror that splits the initial optical path in two. Each path is then equipped with a unique monochromatic filter (associated with an equivalent wavelength) and this system is used as a bichromatic pyrometer. This method is well suited to estimate the melting temperature of pure metals like iron (1810 K), vanadium (2183 K), and niobium (2742 K) with a relative error smaller than 5% and a good spatial resolution of 25 μm). Vallabh and Zhao [44] used the same reasoning to study the melt pool during Laser Powder Bed Fusion. The initial optical path is divided into two paths, first filtered at two different wavelengths and then merged to get a unique output signal with a single high-speed camera. Despite being highly accurate, these two methods require a particular set-up to split the initial optical path, which might not be easily adjustable to any process. Finally, in all the studies above, the exposure time (the time during which the shutter stays open) is an important parameter. Low exposure times make it possible to observe high-temperature areas at the cost of under-exposed colder zones. On the contrary high exposure times tends to overexpose hotter areas. Thus a compromise has to be made and it is not possible to observe high thermal gradient areas (especially the transition between the solid and liquid state in the case of welding or additive manufacturing).

To overcome these limitations, a multi-exposure time strategy is introduced in this paper to study **high thermal gradient phenomena**. The solution is **compact** and pairs reliable thermography with **high resolution optical imaging**.

The adopted solution is a two-color pyrometer made of a single CMOS camera with:

- a fine resolution (6,9 $\mu\text{m} \times 6,9 \mu\text{m}$),
- real-time multi-exposure imaging to study high thermal gradient phenomena,
- an RGB filter where 2 out of the 3 channels are used for the bichromatic computation of the temperature.

Its compact size makes it an easily embedded system to study the melt pool area and its outline: the transition and solid zones.

First, some reminders about Planck's law and bichromatic theory are given, and the calibration of the system is detailed. Then, two validation tests in a controlled environment are presented to assess the precision of the camera. The sensitivity of the method to the parameters chosen during the calibration is discussed in section 4. Finally, section 5 is an application of this method on two DED processes (WAAM and LMD-p). Melt pool contour and thermal gradients in the process zone are outlined.

2. Methodology

2.1. Theory

Thermography has a few important properties that are:

- The temperature (T in Kelvin) of an object at a specific wavelength (λ in meters) increases with its luminous flux (*i.e.* its luminance written $L(\lambda, T)$ in $\text{W.m}^{-3}.\text{sr}^{-1}$).
- The emissivity of a surface (ϵ) is its effectiveness to emit a luminous flux.
- A blackbody is a perfect physical body that absorbs all incident radiations. Its luminance is written L^0 and its emissivity is equal to 1 ($\epsilon_0 = 1$).
- A gray body is a physical body that has an emissivity that does not depend on the wavelength ($\epsilon < 1$).

Wien's approximation of Planck's law (Equation 1) gives the luminance of a black body according to its temperature for a given wavelength:

$$L^0(\lambda, T) = \frac{C_1 \lambda^{-5}}{\exp(\frac{C_2}{T\lambda})}, \quad (1)$$

where $C_1 = 2hc^2 \text{ W.m}^{-2}.\text{sr}^{-1}$ and $C_2 = \frac{hc}{k} \text{ m.K}$ are two constants with:

- $h = 6,626 \times 10^{-34} \text{ J.s}$ (Planck's constant),

- $k = 1,3806 \times 10^{-23} \text{ J.K}^{-1}$ (Boltzmann's constant),
- $c = 2,9979 \times 10^8 \text{ m.s}^{-1}$ (the speed of light in vacuum).

It is necessary to make multiple assumptions to evaluate $L(\lambda, T_s)$ (Equation 2) of a random surface. Since all studied objects in this study are metallic, they can be considered opaque with a transmissivity equal to 0 (which means that no radiation can go through these objects (Duvaut [42])). Thus, the measured luminance is only the sum of the emitted and reflected flux through a translucent environment with a transmissivity τ . The reflected flux is the luminance of the external environment at temperature T_{env} that is reflected on the studied surface. In the case of LMD-p, the reflections of the laser are filtered (subsection 2.2).

$$L(\lambda, T_s) = \epsilon_s \times \tau \times L^0(\lambda, T_s) + (1 - \epsilon_s) \times L^0(\lambda, T_{env}). \quad (2)$$

Due to the high difference between the ambient temperature ($T_{env} = 300 \text{ K}$) and the temperatures of the studied phenomena that are over 1000 K, the impact of the reflective luminance is neglected (Araújo [45]). Furthermore, the luminance of a random surface at the temperature T_s is also necessarily equal to the luminance of a blackbody at a different temperature T_0 , so that the luminance is rewritten as in Equation 3.

$$\begin{aligned} L(\lambda, T_s) &= \epsilon_s \times \tau \times L^0(\lambda, T_s), \\ &= L^0(\lambda, T_0). \end{aligned} \quad (3)$$

And with this equality ($L^0(\lambda, T_0) = \epsilon_s \times \tau \times L^0(\lambda, T_s)$), the surface temperature T_s (Equation 4) writes:

$$T_s = \frac{-C_2}{\lambda \times (5 \ln(\lambda) + \ln(L^0(\lambda, T_0)) - \ln(\epsilon_s \tau C_1))}. \quad (4)$$

The temperature T_0 is determined thanks to the calibration procedure that is detailed thereafter (subsection 2.4).

However, in Equation 4, the emissivity of a random surface is rarely known since it depends on many parameters (such as its roughness, orientation, temperature, and the wavelength at which it is measured). The bichromatic method consists in measuring two luminances at two different wavelengths (λ_1 and λ_2) and writing the ratio of the emissivities. Then for the same surface at the temperature T_s :

$$\begin{cases} L^0(\lambda_1, T_1) = \epsilon_s(\lambda_1) \times L^0(\lambda_1, T_s), \\ L^0(\lambda_2, T_2) = \epsilon_s(\lambda_2) \times L^0(\lambda_2, T_s). \end{cases}$$

With Planck's law (Equation 1), calculating the ratio of $L^0(\lambda_1, T_1)$ over $L^0(\lambda_2, T_2)$ gives the temperature T_s :

$$T_s = \frac{C_2(\frac{1}{\lambda_2} - \frac{1}{\lambda_1})}{5 \ln(\frac{\lambda_1}{\lambda_2}) + \ln(\frac{L^0(\lambda_1, T_1)}{L^0(\lambda_2, T_2)}) + \ln(\frac{\epsilon_s(\lambda_2)}{\epsilon_s(\lambda_1)}) + \ln(\frac{\tau(\lambda_2)}{\tau(\lambda_1)})}. \quad (5)$$

It is possible to make the assumption of a gray body behavior on a narrow waveband on which the emissivity is constant ($\epsilon_s(\lambda_i) = \epsilon_s$) so that: $\frac{\epsilon_s(\lambda_2)}{\epsilon_s(\lambda_1)} = 1$. Besides, the transmissivity of the environment between the camera and the surface

(which is air or translucent gas) is assumed constant too: $\frac{\tau(\lambda_2)}{\tau(\lambda_1)} = 1$. This paper aims at measuring the temperature with a CMOS RGB camera, where two of the three channels will be used in Equation 5.

2.2. Description of the thermal measurement device

The device used is a compact high-performance camera (IOI Victorem 51B136) with a good spectral response in the near-infrared (Figure 1). This CMOS camera is equipped with the Sony IMX250 sensor and an infrared and Bayer filter (to get RGB pictures). The maximum resolution of the camera is 2464×2056 pixels of size $6.9 \mu\text{m} \times 6.9 \mu\text{m}$.

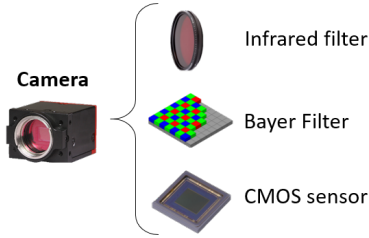


Figure 1: Structure of the camera.

The spectral response of all these components is known through manufacturer data (Figure 2), and the theoretical intensity radiated by a surface (I_{th}) is written:

$$\begin{aligned} I_{th-channel} &= \int_{\lambda_0}^{\lambda_1} i_{th-channel}(\lambda) d\lambda, \\ &= \int_{\lambda_0}^{\lambda_1} L(\lambda, T) \times B(\lambda) \times IR(\lambda) \times \eta(\lambda) d\lambda, \quad (6) \\ channel &= \{red, green, blue\}. \\ &= h(T, \lambda). \end{aligned}$$

With:

- $B(\lambda)$, the efficiency of the Bayer filter according to the wavelength λ ,
- $IR(\lambda)$, the efficiency of the infrared filter,
- $\eta(\lambda)$, the efficiency of the sensor,
- λ_0 and λ_1 the lower and upper limits of the waveband domain.

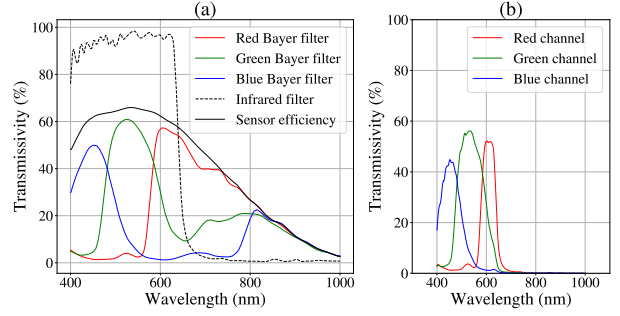


Figure 2: (a) Individual spectral response of the components. (b) Global spectral response for each channel of the camera, data from manufacturer.

With Equation 6, it is possible to predict the theoretical intensity of a blackbody at a temperature T , measured with the camera. The spectral responses of the filters and the sensors are known, and its luminance $L^0(\lambda, T)$ is computed with Equation 1. Figure 3 shows the intensity $I_{th-channel}(\lambda)$ of a blackbody at three different temperatures (1000 K, 1500 K and 2500 K). The camera sensor integrates the area beneath the curve, and the theoretical intensity ($I_{th-channel}$) of each channel corresponds to the hatched surface (the integral of $i_{th-channel}$).

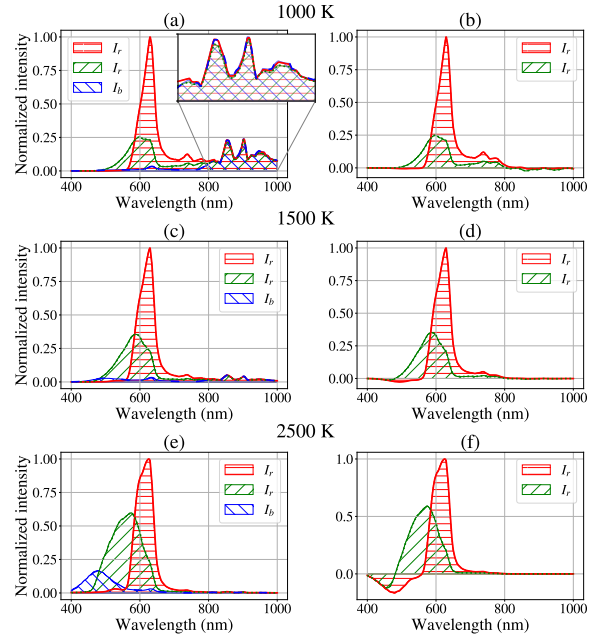


Figure 3: Normalized intensities via the spectrum of each channel at 1000 K (a), 1500 K (c) and 2500 K (e). Normalized intensities via the spectrum of red and green channels corrected by the blue at 1000 K (b), 1500 K (d), and 2500 K (f).

For low temperatures around 1000 K (a), the intensity signal received through the blue channel (I_{blue}) is much lower than the red (I_{red}) and green (I_{green}) ones in the visible range from 400 to 800 nm. The signal above is due to the imperfection of the infrared filter that does not cut 100% of

the signal above 800 nm. The zoom in on (a) shows that it is identical in the 3 channels. Therefore, the blue channel is used as the last filter to remove the signal above the visible range, and also to correct the measured intensity in Equation 7 for the red (I_{red}^{cor}) and green (I_{green}^{cor}) channels (b):

$$\begin{cases} I_{red}^{cor} = I_{red} - I_{blue}, \\ I_{green}^{cor} = I_{green} - I_{blue}. \end{cases} \quad (7)$$

At medium temperatures around 1500 K (c), the correction by the blue channel brings very little variation to the measures of the red and green channels (d).

From 2200 K to above (e), the signal of the blue channel increases, and the corrected intensities in the red and green channel (f) will be underestimated values of the corresponding intensities. For both studies presented at the end of this paper (LMD-p and WAAM), the maximum temperature is below this threshold.

The impact and validity of the correction by the blue channel are detailed thereafter.

2.3. Multi-exposure time

Each picture is made of pixels encoded on 8 bits that can take a value between 0 and 255. An overexposed area is equivalent to a zone where the sensor is saturated and the values of the pixels are close to 255. On the contrary, when the values of pixels tend to 0, the area is underexposed. To catch all the contrast and brightness of the DED processes, the high dynamic range method consists in taking multiple images of the same scenery at different exposure times (Kang et al. [46]). The exposure time is the physical parameter that regulates this phenomenon. When the shutter stays open a very short time (*i.e.* a short exposure), the number of transmitted photons is lower which is interesting to observe very bright phenomena while avoiding overexposition.

This strategy is very efficient to observe spatially high-temperature gradients, unlike spatially uniform temperature field where a single exposure time is sufficient to get the temperature everywhere. Taking multiple successive pictures at very short time intervals makes it possible to assemble a consistent median picture without over/under exposures.

The temperature field is assumed stationary (temporally constant) during the time Δt where n pictures are taken with a different exposure time. This aspect is discussed further in this paper for the respective processes (LMD-p and WAAM, section 5).

With 5 exposure times (0.025, 0.075, 0.225, 0.675 and 2.000 ms), it is possible to reconstruct a median picture with temperatures ranging from 1000 to 2500 K (Figure 4).

All images ($I_1; I_2; \dots; I_5$) of dimensions $n \times m$ have a different exposure times ($t_1; t_2; \dots; t_5$) but are encoded on 8 bits with 256 levels. To reconstruct a median picture, a 2D array of dimensions ($n \times m$) is created, and each element corresponds to:

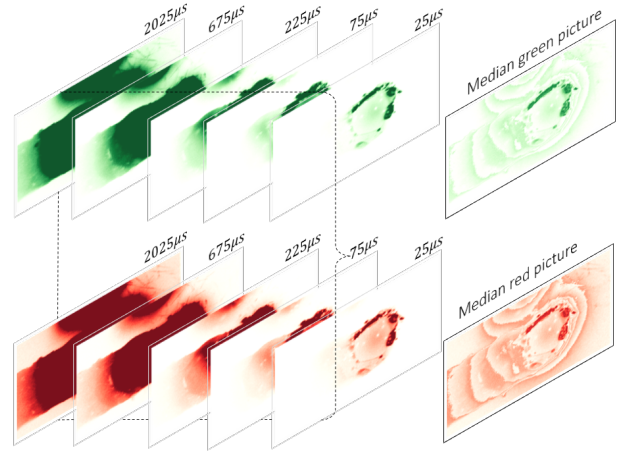


Figure 4: Reconstructed median pictures in the red and green channels.

- The intensity the closest to 126 from all the images (127 corresponds to the median value of the 256 levels of intensity).
- The associated exposure time.

For the example in Figure 4 with 5 pictures, the edge elements of the reconstructed image will be issued from the picture with the longer exposure ($I_1; t_1$) while the center elements will be picked from the picture with the shortest exposure ($I_5; t_5$).

$$\begin{bmatrix} (I_1; t_1) & \dots & (I_1; t_1) \\ \vdots & \ddots & \vdots \\ (I_1; t_1) & \dots & (I_1; t_1) \end{bmatrix}$$

Finally, it has been verified that the intensity evolves linearly with the exposure time. Let I_1 be the intensity of a surface measured with an exposure time t_1 . Then, for the same surface, if the exposure time t_2 is twice t_1 : $I_2 = 2 \times I_1$.

The final reconstructed picture is then normalized and expressed in term of experimental intensity (Equation 8).

$$I_{exp(i)} = I_i / t_i. \quad (8)$$

The index i corresponds to the i^{th} pixel, I_i is the gray level intensity in a single channel (between 0 and 255) and t_i is the corresponding exposure time for the i^{th} pixel.

$$\begin{bmatrix} I_1/t_1 & \dots & I_1/t_1 \\ \vdots & \ddots & \vdots \\ I_1/t_1 & \dots & I_1/t_1 \end{bmatrix}$$

The choice of the exposure times is made according to different criteria, from the most constraining to the less:

1. The duration Δt during which the temperature field is constant greatly impact the number of exposure times, and their values,

2. The wider the exposure times range is, the wider the measured temperature range is too,
3. The more exposure times, the better.

Once these criteria have been studied, the shortest exposure time is set so that the maximum intensity $I_{exp-max}$ times the minimal exposure time t_{min} (*i.e.* the area with the maximum temperature) is less than 240 in terms of gray level so there will be no saturation on the sensor. Then the maximum exposure time t_{max} is set so that $I_{exp-min} \times t_{max}$ is greater than 20 in terms of gray level so the sensor will not be under-exposed. Between t_{min} and t_{max} , the other exposure times are set at regular intervals so that every temperature in the range can be measured. In practice, they are at least two to three times higher than the first one and the overlap can be used to check that the temperature estimation does not depend on the exposure time (*i.e.* the intensity evolves linearly).

2.4. Calibration

The calibration process consists in adjusting the parameters of Equation 5 to reduce the error on the computed temperature. There are two sets of parameters to find in this equation:

- the luminances ($L^0(\lambda_{red}, T_{red})$ and $L^0(\lambda_{green}, T_{green})$),
- the wavelengths (λ_{red} and λ_{green}).

The camera is calibrated on a black body (GHG infrared, RCN1250) and a tungsten ribbon lamp (Osram WI 17 G). The first one is suited for low temperatures (900 to 1470 K) while the other has a higher range (1900 to 2300 K) and they both have an uncertainty of ± 3 K. Both systems are placed perpendicular to the optical axis, and the radiation emitted is measured with the camera.

The luminances depend on the intensities measured with the camera. The objective of the calibration is to find a simple relation between these two parameters. With Equation 6, it is possible to compare the theoretical intensities and the experimental ones measured on the black body and the tungsten ribbon lamp (Figure 5). The luminance of the blackbody is computed with Equation 1. However, the calibration lamp is not a blackbody but has a known emissivity (ϵ_s) as a function of the temperature of the lamp. Its luminance is computed with Equation 2.

The vertical crosses '+' correspond to the experimental values at which the intensity was measured and compared, and the multicolored line is the linear interpolation between the two intensities (Equation 9) where the color stands for the associated temperature.

$$I_{exp-channel} = \alpha_{channel} \times I_{th-channel}. \quad (9)$$

The coefficients α need to be determined for each configuration of the camera (for instance in the LMD-p configuration in section 5, $\alpha_{red} = 257 \times 10^3$; $\alpha_{green} = 263 \times 10^3$). The R^2 correlation coefficient is over 98% for both channels.

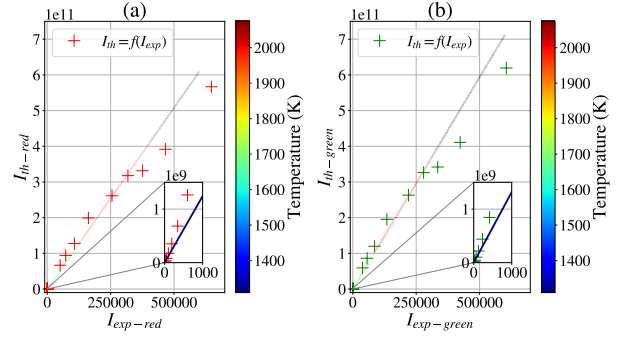


Figure 5: Theoretical intensity in function of experimental intensity in the red (a) and green (b) channels for the optical path used in LMD-p.

These coefficients stand for the optical path of the mounted lens on the camera that is unknown, but they also depend on the parameters of the calibration (2.5) whether the intensities in the red and green channels have been corrected by the blue channel or not.

The goal of this part of the calibration is to estimate the luminances $L^0(\lambda_{channel}, T_{channel})$ of Equation 5. According to the experimental intensity $I_{exp-channel}$. In Equation 6, the theoretical intensity $I_{th-channel}$ is expressed as a function of the temperature T and the wavelength λ ($I_{th-channel} = h(T, \lambda)$).

Let h^{-1} be the inverse function numerically determined that writes: $T = h^{-1}(I_{th-channel})$, with the linear relation between both experimental and theoretical intensities, the temperature is written as a function of the experimental intensity (Equation 10).

$$T_{channel} = h^{-1}(\alpha_{channel} \times I_{exp-channel}). \quad (10)$$

The two temperatures T_{red} and T_{green} are color temperatures which means that they are measured given the black body hypothesis (with an emissivity equal to one). By definition, these temperatures are false because the observed surface is not a black body and the emissivity has to be adjusted. Thus the real temperature estimation can be improved by using these color temperatures as input parameters for the bichromatic equation Equation 11.

Knowing the temperatures T_{red} and T_{green} , the luminances $L^0(\lambda_{red}, T_{red})$ and $L^0(\lambda_{green}, T_{green})$ can be computed with Equation 1 by choosing a couple of initial wavelength ($\lambda_{red}^0 = 650$ nm; $\lambda_{green}^0 = 450$ nm). The choice of these initial wavelengths is arbitrary and influences the rest of the calibration, as explained below. The last missing variables of Equation 5 are the wavelengths λ_{red}^{eq} and λ_{green}^{eq} (Equation 11).

This camera is a low-cost solution for wide field bichromatic sensor, and unlike a pyrometer, it uses two wide wavebands defined in Figure 2 on which the radiated flux is integrated and the optical path of each lens mounted on the camera is unknown. Thus this optimization of the

equivalent wavelengths is needed to reduce the error due to these uncertainties. The bichromatic equation becomes:

$$T_{th} = \frac{C_2 \left(\frac{1}{\lambda_{green}^{eq}} - \frac{1}{\lambda_{red}^{eq}} \right)}{5 \ln \left(\frac{\lambda_{red}^{eq}}{\lambda_{green}^{eq}} \right) + \ln \left(\frac{L^0(\lambda_{red}^0, T_{red})}{L^0(\lambda_{green}^0, T_{green})} \right)}. \quad (11)$$

In Equation 11, the choice of λ_{red}^{eq} and λ_{green}^{eq} is done by minimizing the difference between the theoretical temperature (T_{th}) and the experimental one (T).

The same initial pair of wavelength is chosen ($\lambda_{red}^0 = 650$ nm; $\lambda_{green}^0 = 450$ nm), and the equivalent pair is the one that minimizes $|T - T_{th}|$ under the following constraints:

- $\lambda_{red}^{eq} > \lambda_{green}^{eq}$,
- $\lambda_{red}^{eq} \in [400; 800]$ nm,
- $\lambda_{green}^{eq} \in [400; 800]$ nm.

Each pair of equivalent wavelengths depends on the lens that is mounted on the camera. For the two lenses tested in this work, the absolute error (Equation 12) is lower than 5 K (Figure 6).

$$E_{abs} = |T_{measured} - T_{camera}|. \quad (12)$$

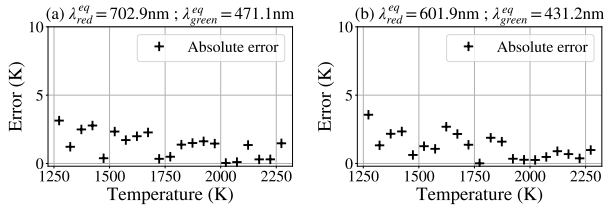


Figure 6: Absolute error with a different lens mounted on the camera (a) Nikon ED af micro nikkor 200mm (WAAM); (b) Precitec ZO YW30 CAM90° YW50 660 (LMD-p).

The influence of the choice of the initial wavelengths is investigated later in this article (subsection 4.1).

2.5. Calibration's parameters and discussion

The calibration process is different for every lens mounted on the camera. This section investigates the impact of the correction by the blue channel and the impact of optimizing or not the equivalent wavelength. On Table 1, the Mean Sum of Squared Differences (MSSD, in Equation 13) on all the temperature range is investigated.

$$MSSD = \frac{1}{N} \times \sum_{n=1}^{n=N} (T_{measured} - T_{camera})^2, \quad (13)$$

where N is the total number of experimental measures. High values of MSSD means that $T_{measured}$ and T_{camera} are very different in all the temperature range.

Mean sum of squared differences (K^2)	Without correction by the blue channel	With correction by the blue channel
With $\lambda^{eq} = \lambda^0$	19128	185.2
By optimizing λ^{eq}	39.7	0.5

Relative difference between the initial and equivalent wavelength		
$\Delta\lambda = \lambda^{eq} - \lambda^0$	$\Delta_{red} = +175.2nm$ $\Delta_{green} = +62.9nm$	$\Delta_{red} = +52.9nm$ $\Delta_{green} = +21.1nm$

Table 1

Mean sum of squared difference between the theoretical temperature and the experimental one after the calibration of the camera for the optical path used in LMD-p.

The numerical values depend on the lens mounted on the camera, but the subtraction of the blue channel and the optimization of the equivalent wavelength are two important features that improve the precision of the temperature measurement.

2.6. Experimental measure of the temperature

To summarize, the measure of the temperature is a 6 steps process (Figure 7). The first 2 steps consist in calibrating the camera:

1. Finding the correlation between the theoretical and experimental intensities (Figure 5).
2. Optimizing the equivalent wavelength to reduce the computational error (Figure 6).

Then, once the acquisition of multiple RGB pictures at different exposure times is done, the 2 next steps involve image processing:

3. Reconstruction of a median picture (Figure 4).
4. Correction of the experimental red and green intensities by subtracting the blue channel (Figure 3).

Finally, the last 2 steps are the computation of the temperature:

5. Estimation of the luminances with the known theoretical intensities which has been correlated with experimental ones (Equation 9).
6. Computation of the temperature (Equation 11).

This is the process to get thermal imaging from multiple RGB pictures at different exposure times. The calibration has to be done for every lens mounted on the camera.

3. Validation of the method

3.1. Induction heating in the solidus

The camera has been used in a controlled environment to monitor the heating temperature of stainless steel (316L) tubes by induction. This experiment aims to compare the temperature measured with an accurate method (type K thermocouples), and the temperature estimated with the camera to validate the method. The device (Figure 8) was designed

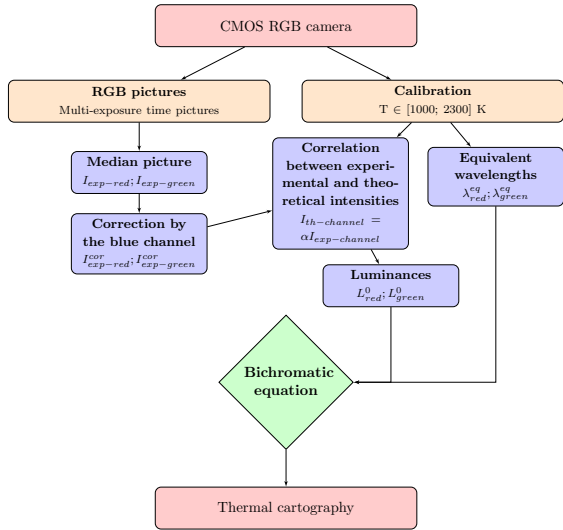


Figure 7: Flowchart of the process for thermal cartography.

years ago to investigate the behavior of Zr-4 tubes in case of an accident in nuclear reactor vessel (Campello et al. [47], Tardif et al. [48]).

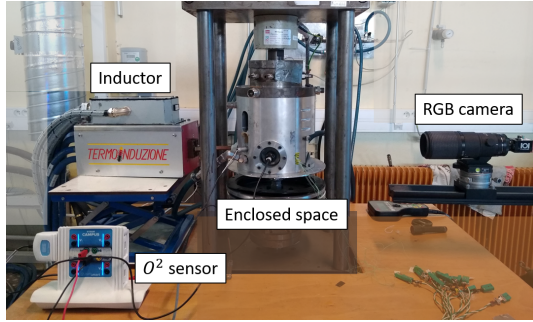


Figure 8: Experimental setup.

In the present experiment, the tube's diameter is $\varnothing 10\text{mm}$ with a thickness of 3 mm, and they are heated by induction in an open loop tension monitored by the power supply. Besides, the oxygen rate is continuously measured.

The induction coils delivers an axisymmetric temperature in the tube. The same camera (IOI Victorem 51B136) equipped with a 200 mm focal lens (AF Micro-Nikkor 200 mm) is used to observe it. Without argon in the enclosed space, the oxygen rate is constant and equal to 20.8%. When the environment is filled with argon, the oxygen rate drops to 0.2% under the initial conditions at the outside air temperature. Additionally to the camera, spot-welded type K thermocouples (wire diameter of 0.2 mm) are used to monitor temperatures lower than 1470 K with a relative uncertainty (ΔTC) of $\pm 1\%$ (Figure 9).

By increasing the tension with the power supply, the induced temperature increased to reach more than 1500 K on the tube whose fusion temperature is around 1650 K.

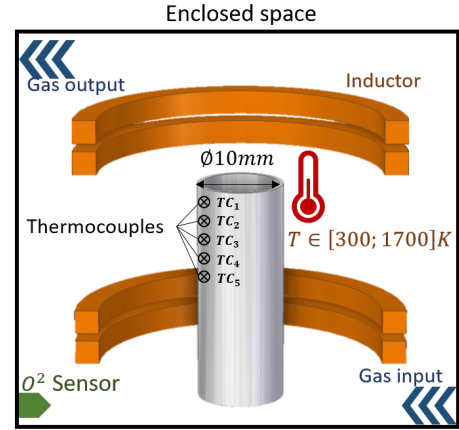


Figure 9: Internal schematic of the experimental setup.

The temperature increases from 1170 K to 1500 K at 10 K.s^{-1} . Seven exposure times are chosen for this experiment: 0.050, 0.100, 0.200, 0.500, 1.000, 2.000 et 4.000 ms. The minimal temperature that can be studied with the longest exposure time is 1170 K. Over the time gap between two successive takes, the temperature increases by 0.08 K which is low enough to make the stationary thermal field hypothesis. The temperature is measured at different heights (h) with the camera (T_{cam_h}), matching the positions of the thermocouples (T_{TC_h}) and the absolute error (Equation 14) is displayed on Figure 10.

$$E_{abs_h} = |T_{TC_h} - T_{cam_h}| \quad (14)$$

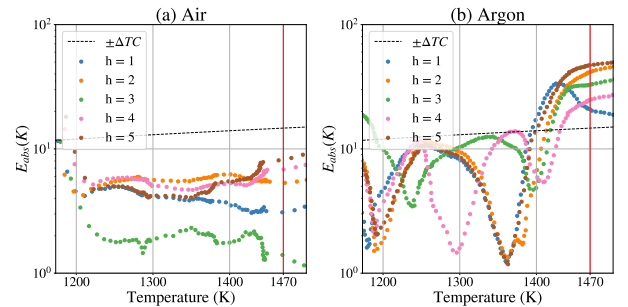


Figure 10: Absolute error in an environment (a) without argon and (b) with argon (logarithmic scale). ΔTC is the uncertainty of the thermocouples.

Below 1200 K, the radiation is not enough compared to the camera's spectral response. Below 1400 K in both environments, the absolute error is below 10 K, while the relative uncertainty of the thermocouples (the dotted black line) is slightly over 10 K. Between 1400 K and 1500 K, in the environment filled with argon, the error increases for every thermocouple which means that there is a common factor affecting the camera results. It is thought that a thin layer of

oxide forms at 1400 K and distorted the temperature measured on the camera whereas an oxide layer with stabilized emissivity spectrum is already present at 1200 K under air. In a nutshell, the formation of oxide is a source of error in optical temperature measurement because the emissivity varies non-linearly on the considered waveband and the gray body assumption does not hold anymore (Equation 5). However, once the oxide layer is thick enough (a few micrometers), the gray body assumption holds. Shi et al. [49] modeled the effect of surface oxidation on the emissivity for temperatures ranging from 800K to 1100K on the same material, stainless steel 316L. They showed that the formation of a very thin layer of oxide creates oscillations in the spectral emissivity, that disappear once the layer is optically thick. Li et al. [50] also pointed out this kind of behavior on a Ti-6Al-4V alloy where strong oscillations of the emissivity were observed during the transient oxidation period. In order to reduce the uncertainty due to the brief moment of surface oxidation, it is possible to pre oxidized the studied surface. When this is not an option, for instance during additive manufacturing, the solution consists in inerting the observed area. Although it won't prevent some oxide spots from appearing on the surface, this will only create small local errors and won't prevent a global visualization of the temperature and its gradient (on Figure 24, some oxide spots are visible inside the red isotherm). This means that the results obtained with the camera as a non-contact measurement are very accurate in this range of temperature ($T \in [1200; 1500]$ K).

3.2. Fusion temperature of elementary bodies

To validate this system above 1500 K near the transition between the solid and liquid phases, the melting of rods made of elementary materials is studied. Similar experiments were conducted by Morville et al. [51] to study the shape of the top of the rod once it starts melting, and by Monier et al. [43] to study the position of the melting front on the rods. The fusion temperature of elementary bodies is accurately known and can be compared to the one computed on the images obtained.

In this study, a diode laser (Laserline LMD 1000-100) with a wavelength of 1070 nm is used to heat the top of a metallic rod of 2 mm diameter. The camera is mounted above the laser nozzle on a camera lens specially designed for the laser head focusing optics (Precitec focusing optics YW52). At the focal distance, the laser beam diameter is 1.2 mm. The laser nozzle and the rod are placed within an enclosed space so it can be filled with argon (Figure 11).

Vanadium rods of 2 mm diameter and 25 mm length are used for this experiment. Their properties are well known and summarized in Table 2.

Thermal properties	Vanadium
Fusion temperature (K)	2183
Density ($kg.m^{-3}$)	6100
Thermal conductivity ($W.m^{-1}.K^{-1}$)	30.7

Table 2
Thermal properties of Vanadium (GoodFellow [52]).

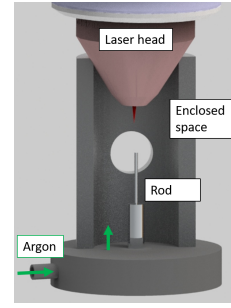


Figure 11: Experimental setup for the fusion of elementary bodies.

To reach the melting point, the laser power is set to 350 W for 2 s. For each rod, 6 exposure times are selected (0.025, 0.050, 0.100, 0.200, 0.500 et 1.000 ms) and a succession of images is taken every 40 ms. The goal is to study the beginning of the fusion when the rod is barely melted, and right after the laser stops to observe its fusion and its solidification (Figure 12).

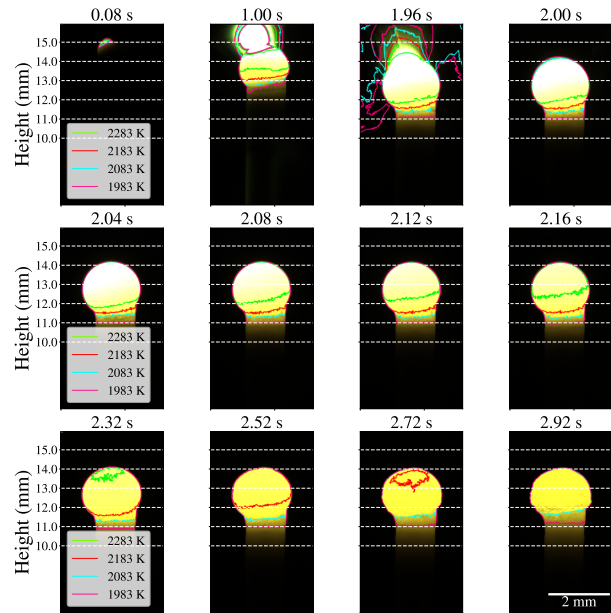


Figure 12: Evolution of the temperature along the rod.

RGB pictures represent the vanadium rod at the beginning of the experiment ($t = 0.08$ s), right before the laser stops ($t < 2.00$ s) and just after ($t > 2.00$ s). The colored contours stand for the area on the picture where the temperature is over a certain threshold. The red one corresponds to the fusion temperature (2183 K), the green one to 100 K above, the cyan one to 100 K below, and the pink one to 200 K below. As the laser heats the top of the rod, a spherical droplet starts to form, which means that this part of the rod is liquid. The limit between the liquid droplet and the solid part of the rod is represented by the red isotherm (at 2183 K). This isotherm precisely extends the contours of

the sphere at 2.00 s. During the 0.16 next seconds, the green 2283 K isotherm slowly climbs back up the rod while the three other isotherms remain at the same position. The fact that the isotherm at the fusion temperature remains stable during the natural cooling of the rod confirms that the upper part is liquid, with a temperature slightly higher. Besides, the shape of the droplet remains perfectly spherical until 2.32 s due to surface tension, which is a sign that it is still liquid. Once the red isotherm starts moving (after 2.52 s), the surface of the droplet becomes irregular, which means it is solid.

This experiment shows that this bichromatic sensor is a reliable method to estimate high temperatures both in the solid and liquid phases. Besides, the camera resolution is fitted to observe the macroscopic movements of the melted zones (during the fusion or the solidification of the rod). This is interesting for dynamic processes such as DED where the shape of the melt pool evolves constantly.

4. Analysis of the uncertainties

4.1. Uncertainties and sources of errors

In the theoretical expression of the bichromatic temperature (Equation 5), two parameters may be sources of errors:

- The choice of the initial wavelengths.
- The surface emissivity (*i.e.* the gray body hypothesis).

Their effect on the estimation of the temperature is studied at the calibration step. New calibrations are performed with:

- New initial wavelengths (λ^0 in Equation 11).
- An emissivity ratio varying between 0.9 and 1.1 ($\epsilon = \frac{\epsilon_s(\lambda_{red})}{\epsilon_s(\lambda_{green})}$ in Equation 5).

The equivalent wavelength evolves linearly with the initial wavelength (Figure 13). This picture is in 2 dimensions because the green initial wavelength has no impact on the computation of the red equivalent wavelength (and vice versa).

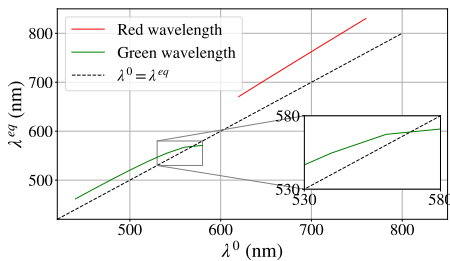


Figure 13: Equivalent wavelengths as a function of initial wavelength for the optical path used in LMD-p.

For every couple of initial wavelengths ($(\lambda_{red}^0; \lambda_{green}^0)$) and their associated equivalent wavelengths, the maximum error during the calibration process is computed (Figure 14).

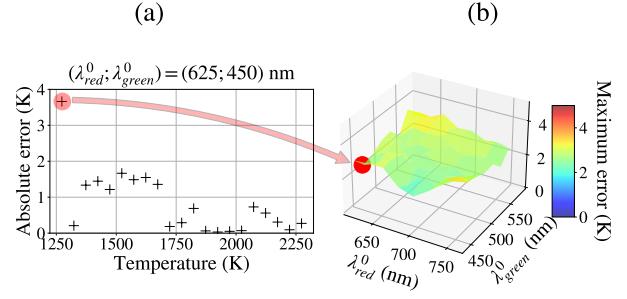


Figure 14: (a) Absolute error for a particular couple of initial wavelengths; (b) Maximum error for different couples of initial wavelengths.

The maximum error varies between 2 and 5 K, which means that the choice of the initial wavelength has nearly no impact on the estimated temperature.

The impact of the emissivity ratio is studied for a given couple of wavelengths. The calibration is performed with a ratio varying between 0.9 and 1.1, and the maximum error is associated with the corresponding ratio (Figure 15).

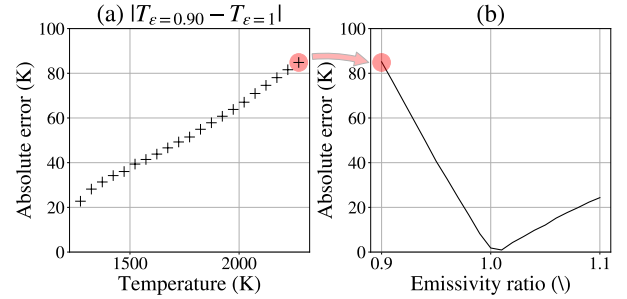


Figure 15: (a) Absolute error for an emissivity ratio of 0.90; (b) Maximum error for different ratios.

The gray body assumption is a strong hypothesis because the emissivity ratio strongly impacts the temperature calculation. A variation within the range of $\pm 10\%$ can introduce a relative error up to 80 K. Besides, the emissivity is influenced by a lot of parameters including the surface state, its inclination, and the optical path. Thus, in experimental conditions, external parameters such as oxidation, powder ejections, or melt pool dynamics are a constant source of error which may induce a few variations in the measured temperature.

5. Melt pool thermal cartography in DED manufacturing

5.1. Melt pool temperature in LMD-p

The thermal imaging system introduced in this paper is very compact and can be easily adjusted on any setup. To study the melt pool during LMD-p, it was put on a 6-axis robot (Staubli RX160) equipped with :

- A diode laser (Laserline LMD2000) with a wavelength varying between 900 and 1200 nm and a beam diameter of 1.4 mm.
- A set of outer and inner nozzles (Precitec - ZM YC50 DAS 0.5 II and ZM YC50 DIS II).
- A powder feeder (Oerlikon Twin 150) with 2 distinct tanks with the option to use different materials.
- An ATEX dust extraction system to avoid powder residues in the cabin.
- A camera lens 90° with an optical 660 nm filter (Precitec ZO YW30 CAM90° YW50 660).

The camera is mounted co-axially to the laser nozzle on the camera lens and gives an upside view of the zone being melted by the laser (Figure 16).

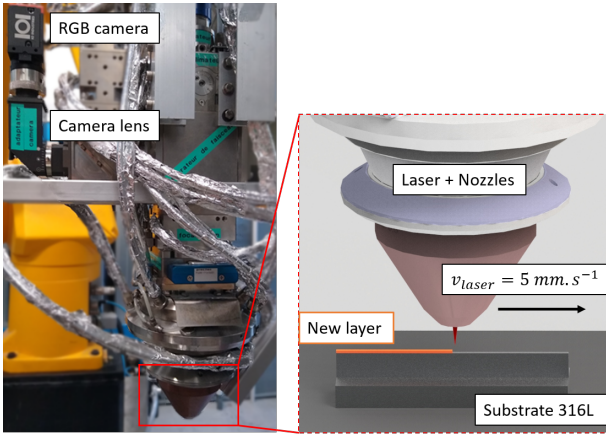


Figure 16: LMD-p experiment for melt pool imaging.

The 316L stainless steel powder is brought as a fine powder (oerlikon metco, metco clad 316L-Si) on the substrate which is also in 316L stainless steel. The powder flow, the laser scan speed and the laser power are kept constant ($Q_{powder} = 3,4 \text{ g.min}^{-1}$; $P_{laser} = 250 \text{ W}$; $v_{laser} = 5 \text{ mm.s}^{-1}$). Seven exposure times are chosen for this experiment: 0.025, 0.050, 0.100, 0.200, 0.500, 1.000 and 2.000 ms, and one picture is taken every 160 ms (Figure 17).

Each column corresponds to a set of pictures taken at very short time intervals but with a different exposure time. The top pictures are overexposed at their center which is the hottest region of the melt pool. However, it is possible to see a hot trail behind the melt pool which is the substrate that is in a solid phase state. Combining the 7 pictures makes it possible to study the temperature in and around the melt pool although there are high thermal gradients.

It is only possible to combine all the pictures if the camera's field of view is stationary throughout the acquisition (*i.e.* all the pictures at different exposure times are taken simultaneously). With a single camera, all n pictures are taken successively during a time Δt , and the assumption that

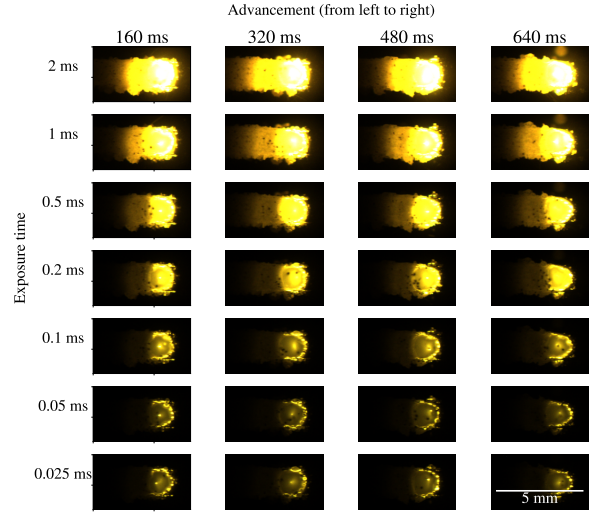


Figure 17: Successive pictures of the melt pool with all their exposure times.

the temperature field is constant during Δt has to be made to recombine these n pictures. For this DED process, the laser velocity is 5 mm.s^{-1} , and $\Delta t = 3 \text{ ms}$. Since the camera is attached to the laser, the maximal displacement while the pictures are taken is $1.5 \mu\text{m}$ which is nearly a thousand times lower than the melt pool width. In these conditions, the hypothesis of a constant temperature field is valid.

Figure 18 (a) is a reconstructed picture in terms of intensity (through the red channel).

Figure 18 (b) is the same image in terms of temperature. Below these, the intensity and temperature profiles of the red line along the wall are plotted. Overall, the intensity and the temperatures follow the same trend, when the first increase, it means that this area is hotter.

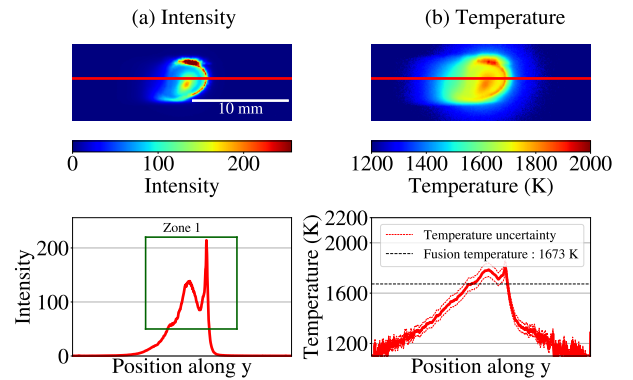


Figure 18: Evolution of (a) the intensity and (b) the temperature along the melt pool.

On the temperature diagram, the fusion temperature of the stainless steel 316L is represented by the dark dotted line (1673 K). Thus, this method provides an efficient way of knowing both the melt pool temperature and its shape.

Finally, zone 1 in the green box in Figure 18 (a) is a bit particular because there is a huge drop in terms of intensity (that translates into a temporary decrease in the temperature). This is counter-intuitive because the center of the melt pool should be hotter than its edges. Smurov et al. [31] had a similar effect on their temperature profiles obtained via an infrared camera. These non-monotone effects indicate substrate oxidation in the heat-affected zone around the melt pool that results in high emissivity variations.

Since the fusion temperature of stainless steel 316L is known (1673 K), it is possible to identify the shape of the melt pool thanks to thermal imaging. Figure 19 shows the thermal cartography during the process (a), and five isotherms (b) 100 K and 200 K below and above the fusion temperature. The image processing was carried out in python thanks to the OpenCV library (Bradski [53]).

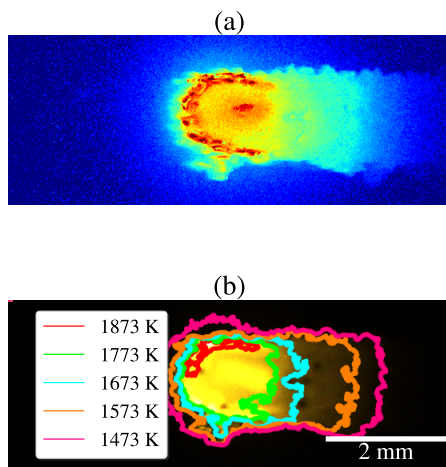


Figure 19: (a) Thermal cartography of the melt pool and its surroundings in LMD-p. (b) Melt pool contour and other isotherms.

With thermal cartography, it is easy to identify isotherms in the pictures. The cyan one highlights the melt pool contour while the 4 others give a simplified view of the thermal gradients in both the solid and liquid areas.

Finally, this experiment on LMD-p is interesting because it shows the flexibility of the camera to study the melt pool, its edges, and the solid area of the manufactured part. The fine resolution of the sensor also provides insights into the melt pool shape which could be the first step of a closed-loop control process to improve the quality of AM parts.

5.2. Melt pool temperature in WAAM

Figure 20 shows the installation used for the WAAM process. It is a YASKAWA MA1440 robot and a Fronius TPS CMT 4000 advanced welding station, using the 1357 CMT synergic law provided by Fronius, with the following parameters:

- A steel wire of 1.2 mm in diameter is used for the experiment (OK Aristorod 12.50).

- A wire-feed speed (WFS) of $3500 \text{ mm}\cdot\text{min}^{-1}$.
- A travel speed (TS) of $400 \text{ mm}\cdot\text{min}^{-1}$.
- A shielding gas made of argon (18%) and CO_2 (82%) with a gas flow of $18 \text{ L}\cdot\text{min}^{-1}$.

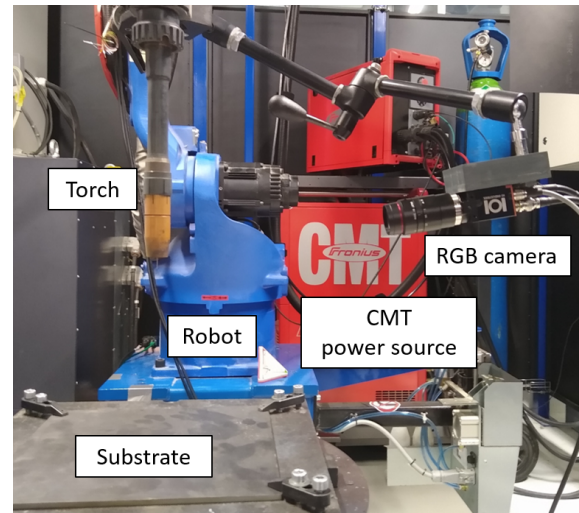


Figure 20: WAAM equipments.

The camera is fixed on the torch and provides a side view of the part being produced. WAAM is a sequential process, with a discontinuous input of matter. The wire leaves the torch until it is in contact with the substrate, creating an electric arc. At that moment, the end of the wire is melted due to the important heat input, and a droplet is deposited onto the substrate. At the same time, the wire goes up (in the opposite direction) for a fixed amount of time before leaving the torch again. A succession of 2 pictures at 2 different exposure times is taken between 2 electric arcs (Figure 21).

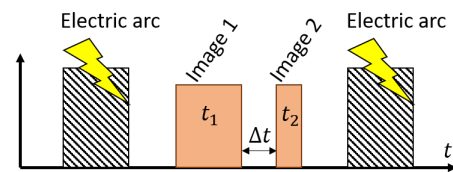


Figure 21: Image acquisition between two electric arcs in WAAM.

The two successive images are taken at an interval Δt of 2 ms. The camera is once again attached to the torch so the maximal displacement, while the pictures are taken, is $1.7 \mu\text{m}$ which is a thousand times lower than the melt pool width. In these conditions, the hypothesis of a constant temperature field is once again valid. Only two exposure times are chosen for this experiment: 0.20 and 0.04 ms, and one set of images is taken every 120 ms (Figure 22).

Figure 23 (a) is a reconstructed picture in terms of intensity through the red channel, and its highest value is

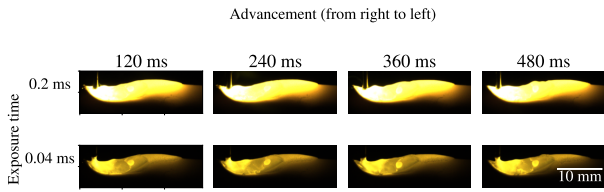


Figure 22: Successive pictures of the melt pool with all their exposure times (WAAM).

255, which means that the camera sensor was saturated at the lowest exposure time. Indeed, the saturated zone is on the spot where the wire enters in contact with the wall, where the local temperature far exceeds the average temperature of the melt pool (more than 3000 K, Cadiou et al. [54]). This means that the estimated temperature in this area will be underestimated by the camera (since the intensity could have been greater).

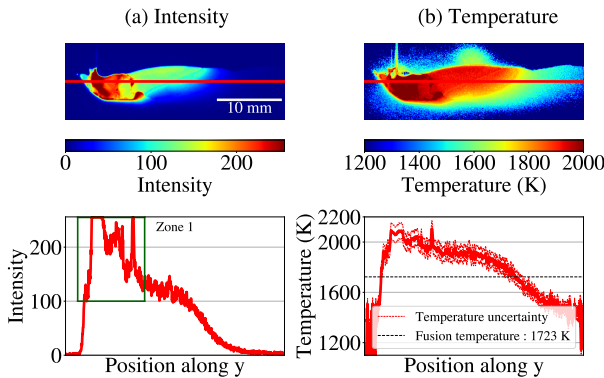


Figure 23: Evolution of (a) the intensity and (b) the temperature along the melt pool during the WAAM process.

Figure 23 (b) is the same image in terms of temperature. As expected, the highest temperature is reached in the contact area between the wire and the wall. However, the temperature is not monotonous along the melt pool with random peaks (zone 1). These anomalies are once again due to the oxidation of the surface of the wall, which generates high emissivity variations.

The fusion temperature of welding wire is around 1723 K so once again, it is possible to draw the contour of the melt pool, but also contours at temperatures below and above (± 200 and 100 K).

In Figure 24, 5 contours are drawn on two RGB pictures taken successively at different exposure times. The fact is that the pictures are not taken exactly at the same time, but with a time gap of 2 ms. Although the temperature field is supposed constant during this short amount of time, it is clear that the liquid surface of the melt pool is highly dynamic, and the contours, despite being the same in both pictures, highlight the zone where the melt pool moved. Finally, this image shows the assets of the full-field sensor introduced in this paper since it is possible to study the

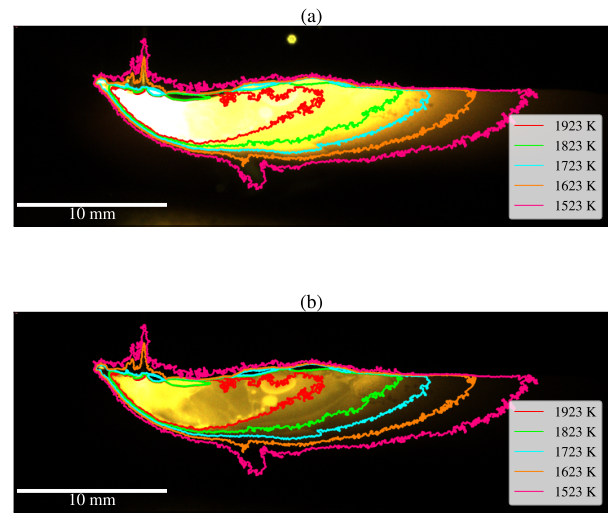


Figure 24: Contour of the melt pool and other isotherms in WAAM, drawn on (a) the longest exposure time (0.20 ms) and (b) the shortest exposure time (0.04 ms).

temperatures of areas both liquid and solid, and with high thermal gradients.

5.3. Data availability

Experimental datas for subsection 3.1, subsection 3.2, subsection 5.1 and subsection 5.2 are available openly [55].

6. Conclusion

A method to measure the temperature with a high gradient area has been presented in this work. Based on a compact CMOS RGB camera in the visible waveband, it uses the bichromatic principle to remove emissivity and transmissivity issues. Wavelength optimization for a fixed temperature range is the key parameter of the calibration to ensure minimal errors. The gray body assumption is valid in a controlled environment but can introduce small errors with external perturbations such as oxides, or uneven surfaces. Thanks to this camera, the temperature of the nearby liquid and solid zones within the range of 1000 K to 2500 K has been studied successfully which makes it a nice tool to follow a melt front and estimate thermal gradients in the heat affected zone that are very valuable for metallurgists. Furthermore, the good spatial and temporal resolutions of the camera make it a good fit to test a process quality (during welding or additive manufacturing) with the option to get both a thermal cartography of the melt pool and its morphology. This method highly depends on the chosen exposure times. Very fast phenomenon can be studied with very short exposure times, but the limiting factor will be the frame rate of the camera, that is the frequency at which consecutive pictures are captured. Currently, this process is being improved to make it faster and integrate it into a closed control loop in the DED processes. The optimization in the

choice of the exposure times and better signal processing are investigated leads.

CRedit authorship contribution statement

Loïc Jegou: Methodology, Validation, Investigation, Writing - Original Draft. **Joël Lachambre:** Conceptualization, Software, Methodology, Investigation, Resources. **Nicolas Tardif:** Conceptualization, Methodology, Supervision, Project administration, Writing - Review & Editing, Funding acquisition. **Mady Guillemot:** Resources. **Anthony Dellarre:** Resources. **Abderrahime Zaoui:** Resources. **Thomas Elguedj:** Supervision, Writing - Review & Editing, Funding acquisition. **Valerie Kaftandjian:** Supervision, Writing - Review & Editing, Funding acquisition. **Nicolas Beraud:** Supervision, Resources, Funding acquisition.

Acknowledgement

This work was partially supported by the institute Carnot Ingénierie@Lyon through the TORTELLINI project and by ANR through the METALIC project ANR-21-CE10-0003, these supports are gratefully acknowledged. The authors would like to thank Cyril Bordreuil from LMGC (Univ. Montpellier, CNRS, 34090, Montpellier, France) for lending the calibration lamp and his insightful discussions. The authors also thank Philippe Chaudet from Lamcos for his help in setting up the experiments.

References

- [1] B. Berman, 3-d printing: The new industrial revolution, *Business horizons* 55 (2012) 155–162.
- [2] W. E. Frazier, Metal additive manufacturing: a review, *Journal of Materials Engineering and performance* 23 (2014) 1917–1928.
- [3] D. Svetlizky, M. Das, B. Zheng, A. L. Vyatskikh, S. Bose, A. Bandyopadhyay, J. M. Schoenung, E. J. Lavernia, N. Eliaz, Directed energy deposition (ded) additive manufacturing: Physical characteristics, defects, challenges and applications, *Materials Today* 49 (2021) 271–295.
- [4] S. W. Williams, F. Martina, A. C. Addison, J. Ding, G. Pardal, P. Colegrove, Wire+ arc additive manufacturing, *Materials science and technology* 32 (2016) 641–647.
- [5] B. Wu, Z. Pan, D. Ding, D. Cuiuri, H. Li, J. Xu, J. Norrish, A review of the wire arc additive manufacturing of metals: properties, defects and quality improvement, *Journal of Manufacturing Processes* 35 (2018) 127–139.
- [6] J. J. Lewandowski, M. Seifi, Metal Additive Manufacturing: A Review of Mechanical Properties, *Annual Review of Materials Research* 46 (2016) 151–186. doi:10.1146/annurev-matsci-070115-032024.
- [7] M. Liu, A. Kumar, S. Bukkapatnam, M. Kuttolamadom, A review of the anomalies in directed energy deposition (ded) processes & potential solutions-part quality & defects, *Procedia Manufacturing* 53 (2021) 507–518.
- [8] C. Wang, X. Tan, S. Tor, C. Lim, Machine learning in additive manufacturing: State-of-the-art and perspectives, *Additive Manufacturing* 36 (2020) 101538.
- [9] N. Johnson, P. Vulimiri, A. To, X. Zhang, C. Brice, B. Kappes, A. Stebner, Invited review: Machine learning for materials developments in metals additive manufacturing, *Additive Manufacturing* 36 (2020) 101641.
- [10] L. Scime, J. Beuth, Using machine learning to identify in-situ melt pool signatures indicative of flaw formation in a laser powder bed fusion additive manufacturing process, *Additive Manufacturing* 25 (2019) 151–165.
- [11] J. Yuan, H. Liu, W. Liu, F. Wang, S. Peng, A method for melt pool state monitoring in laser-based direct energy deposition based on densenet, *Measurement* 195 (2022) 111146.
- [12] I. Jeon, L. Yang, K. Ryu, H. Sohn, Online melt pool depth estimation during directed energy deposition using coaxial infrared camera, laser line scanner, and artificial neural network, *Additive Manufacturing* 47 (2021) 102295.
- [13] M. Khanzadeh, S. Chowdhury, M. A. Tschopp, H. R. Doude, M. Marufuzzaman, L. Bian, In-situ monitoring of melt pool images for porosity prediction in directed energy deposition processes, *IJSE Transactions* 51 (2019) 437–455.
- [14] E. Eren, S. Kurama, I. Solodov, Characterization of porosity and defect imaging in ceramic tile using ultrasonic inspections, *Ceramics International* 38 (2012) 2145–2151.
- [15] B. Wu, D. Ding, Z. Pan, D. Cuiuri, H. Li, J. Han, Z. Fei, Effects of heat accumulation on the arc characteristics and metal transfer behavior in wire arc additive manufacturing of ti6al4v, *Journal of Materials Processing Technology* 250 (2017) 304–312.
- [16] T. Hauser, R. T. Reisch, P. P. Breese, Y. Nalam, K. S. Joshi, K. Bela, T. Kamps, J. Volpp, A. F. Kaplan, Oxidation in wire arc additive manufacturing of aluminium alloys, *Additive Manufacturing* 41 (2021) 101958.
- [17] P. S. Cook, A. B. Murphy, Simulation of melt pool behaviour during additive manufacturing: Underlying physics and progress, *Additive Manufacturing* 31 (2020) 100909.
- [18] A. Fathi, E. Toyserkani, A. Khajepour, M. Durali, Prediction of melt pool depth and dilution in laser powder deposition, *Journal of Physics D: Applied Physics* 39 (2006) 2613.
- [19] P. Peyre, P. Aubry, R. Fabbro, R. Neveu, A. Longuet, Analytical and numerical modelling of the direct metal deposition laser process, *Journal of Physics D: Applied Physics* 41 (2008) 025403.
- [20] P. Michaleris, Modeling metal deposition in heat transfer analyses of additive manufacturing processes, *Finite Elements in Analysis and Design* 86 (2014) 51–60.
- [21] C. Baykasoglu, O. Akyildiz, D. Candemir, Q. Yang, A. C. To, Predicting microstructure evolution during directed energy deposition additive manufacturing of ti-6al-4v, *Journal of Manufacturing Science and Engineering* 140 (2018).
- [22] M. E. Stender, L. L. Beghini, J. D. Sugar, M. G. Veilleux, S. R. Subia, T. R. Smith, C. W. San Marchi, A. A. Brown, D. J. Dagle, A thermal-mechanical finite element workflow for directed energy deposition additive manufacturing process modeling, *Additive Manufacturing* 21 (2018) 556–566.
- [23] J. Heigel, P. Michaleris, E. W. Reutzel, Thermo-mechanical model development and validation of directed energy deposition additive manufacturing of ti-6al-4v, *Additive manufacturing* 5 (2015) 9–19.
- [24] P. Akbari, F. Ogoke, N.-Y. Kao, K. Meidani, C.-Y. Yeh, W. Lee, A. B. Farimani, Meltpoolnet: Melt pool characteristic prediction in metal additive manufacturing using machine learning, *Additive Manufacturing* 55 (2022) 102817.
- [25] T. Jailin, N. Tardif, J. Desquines, M. Coret, M.-C. Baietto, V. Georghum, Experimental study and modelling of the phase transformation of zircaloy-4 alloy under high thermal transients, *Materials Characterization* 162 (2020) 110199.
- [26] S. J. Wolff, B. Gould, Synchronized in situ x-ray and infrared imaging of laser deposition, *Manufacturing Letters* 31 (2022) 87–90.
- [27] M. Boley, F. Abt, R. Weber, T. Graf, X-ray and optical videography for 3d measurement of capillary and melt pool geometry in laser welding, *Physics Procedia* 41 (2013) 488–495.
- [28] Z. Sun, W. Guo, L. Li, In-process measurement of melt pool cross-sectional geometry and grain orientation in a laser directed energy deposition additive manufacturing process, *Optics & Laser Technology* 129 (2020) 106280.

- [29] B. T. Gibson, Y. K. Bandari, B. S. Richardson, W. C. Henry, E. J. Vetland, T. W. Sundermann, L. J. Love, Melt pool size control through multiple closed-loop modalities in laser-wire directed energy deposition of ti-6al-4v, *Additive Manufacturing* 32 (2020) 100993.
- [30] Y. Ding, J. Warton, R. Kovacevic, Development of sensing and control system for robotized laser-based direct metal addition system, *Additive Manufacturing* 10 (2016) 24–35.
- [31] I. Smurov, M. Doubenskaia, A. Zaitsev, Comprehensive analysis of laser cladding by means of optical diagnostics and numerical simulation, *Surface and Coatings Technology* 220 (2013) 112–121.
- [32] Z. Zhao, Y. Guo, L. Bai, K. Wang, J. Han, Quality monitoring in wire-arc additive manufacturing based on cooperative awareness of spectrum and vision, *Optik* 181 (2019) 351–360.
- [33] J. Xiong, Z. Yin, W. Zhang, Closed-loop control of variable layer width for thin-walled parts in wire and arc additive manufacturing, *Journal of Materials Processing Technology* 233 (2016) 100–106.
- [34] S. K. Everton, M. Hirsch, P. Stravroulakis, R. K. Leach, A. T. Clare, Review of in-situ process monitoring and in-situ metrology for metal additive manufacturing, *Materials & Design* 95 (2016) 431–445.
- [35] S. Liu, P. Farahmand, R. Kovacevic, Optical monitoring of high power direct diode laser cladding, *Optics & Laser Technology* 64 (2014) 363–376.
- [36] K. Yamazaki, E. Yamamoto, K. Suzuki, F. Koshiishi, S. Tashiro, M. Tanaka, K. Nakata, Measurement of surface temperature of weld pools by infrared two colour pyrometry, *Science and Technology of Welding and Joining* 15 (2010) 40–47.
- [37] Y. Rotrou, T. Sentenac, Y. Le Maout, P. Magnan, J. Farré, Near infrared thermography with silicon fpa-comparison to mwir and lwir thermography, *Quantitative InfraRed Thermography Journal* 3 (2006) 93–115.
- [38] T. Jailin, N. Tardif, P. Chaudet, J. Desquines, M. Coret, M.-C. Baietto, V. Georgenthum, Measuring both thermal and kinematic full-fields using a single cmos camera during high temperature tests, *Optics and Lasers in Engineering* 158 (2022) 107107.
- [39] H. Schöpp, A. Sperl, R. Kozakov, G. Gött, D. Uhrlandt, G. Wilhelm, Temperature and emissivity determination of liquid steel s235, *Journal of Physics D: Applied Physics* 45 (2012) 235203.
- [40] R. Kozakov, H. Schöpp, G. Gött, A. Sperl, G. Wilhelm, D. Uhrlandt, Weld pool temperatures of steel s235 while applying a controlled short-circuit gas metal arc welding process and various shielding gases, *Journal of Physics D: Applied Physics* 46 (2013) 475501.
- [41] M. A. Khan, C. Allemand, T. W. Eagar, Noncontact temperature measurement. i. interpolation based techniques, *Review of scientific instruments* 62 (1991) 392–402.
- [42] T. Duvaut, Comparison between multiwavelength infrared and visible pyrometry: Application to metals, *Infrared Physics & Technology* 51 (2008) 292–299.
- [43] R. Monier, F. Thumerel, J. Chapuis, F. Soulié, C. Bordreuil, Liquid metals surface temperature fields measurements with a two-colour pyrometer, *Measurement* 101 (2017) 72–80.
- [44] C. K. P. Vallabh, X. Zhao, Single-camera two-wavelength imaging pyrometry for melt pool temperature measurement and monitoring in laser powder bed fusion based additive manufacturing, *arXiv preprint arXiv:2109.07472* (2021).
- [45] A. Araújo, Analysis of multi-band pyrometry for emissivity and temperature measurements of gray surfaces at ambient temperature, *Infrared Physics & Technology* 76 (2016) 365–374.
- [46] S. B. Kang, M. Uyttendaele, S. Winder, R. Szeliski, High dynamic range video, *ACM Transactions on Graphics (TOG)* 22 (2003) 319–325.
- [47] D. Campello, N. Tardif, J. Desquines, M.-C. Baietto, M. Coret, A. Maynadier, P. Chaudet, Validation of a multimodal set-up for the study of zirconium alloys claddings' behaviour under simulated loca conditions, *Strain* 54 (2018) e12279.
- [48] N. Tardif, M. Coret, A. Combescure, Experimental study of the fracture kinetics of a tubular 16mnimo5 steel specimen under biaxial loading at 900 and 1000 c. application to the rupture of a vessel bottom head during a core meltdown accident in a pressurized water reactor, *Nuclear engineering and design* 241 (2011) 755–766.
- [49] D. Shi, F. Zou, Z. Zhu, J. Sun, Modeling the effect of surface oxidation on the normal spectral emissivity of steel 316l at 1.5 μm over the temperatures ranging from 800 to 1100 k in air, *Infrared Physics & Technology* 71 (2015) 370–377.
- [50] L. Li, K. Yu, K. Zhang, Y. Liu, Study of ti-6al-4v alloy spectral emissivity characteristics during thermal oxidation process, *International Journal of Heat and Mass Transfer* 101 (2016) 699–706.
- [51] S. Morville, M. Carin, M. Muller, M. Gharbi, P. Peyre, D. Carron, P. Le, R. Masson, 2d axial-symmetric model for fluid flow and heat transfer in the melting and resolidification of a vertical cylinder, in: *Proceedings of the COMSOL Conference Paris, Paris, France, 2010*, pp. 17–19.
- [52] GoodFellow, Vanadium properties, <https://www.goodfellow.com/fr/en-us/metal,????> [Online; accessed 18-October-2022].
- [53] G. Bradski, The OpenCV Library, *Dr. Dobb's Journal of Software Tools* (2000).
- [54] S. Cadiou, M. Courtois, M. Carin, W. Berckmans, et al., 3d heat transfer, fluid flow and electromagnetic model for cold metal transfer wire arc additive manufacturing (cmt-waam), *Additive Manufacturing* 36 (2020) 101541.
- [55] L. Jegou, J. Lachambre, N. Tardif, Bichromatique melt pool thermal measurement based on a Red, Green, and Blue camera: application to additive manufacturing processes, 2023. URL: <https://doi.org/10.57745/CM2W0I>. doi:10.57745/CM2W0I.